2016

Nanofiber scaffolds influence organelle structure and function in bone marrow stromal cells

Wojtek Tutak
National Institute of Standards and Technology

Giri Jyotsnendu
National Institute of Standards and Technology

Peter Bajcsy
American Dental Association Foundation

Carl G. Simon Jr.
National Institute of Standards and Technology

Society For Biomaterials

Nanofiber scaffolds influence organelle structure and function in bone marrow stromal cells

Wojtek Tutak,[1,2] Giri Jyotsnendu,[1,3] Peter Bajcsy,[4] Carl G. Simon, Jr.[1]

[1]Biosystems and Biomaterials Division, National Institute of Standards and Technology, Gaithersburg, Maryland
[2]Department of Biomedical Engineering, Indian Institute of Technology, Hyderabad, Yeddumailaram, AP, India
[3]Software and Systems Division, National Institute of Standards and Technology, Gaithersburg, Maryland
[4]American Dental Association Foundation, Gaithersburg, Maryland

Received 25 September 2015; revised 8 December 2015; accepted 10 January 2016
Published online 17 February 2016 in Wiley Online Library (wileyonlinelibrary.com). DOI: 10.1002/jbm.b.33624

Abstract: Recent work demonstrates that osteoprogenitor cell culture on nanofiber scaffolds can promote differentiation. This response may be driven by changes in cell morphology caused by the three-dimensional (3D) structure of nanofibers. We hypothesized that nanofiber effects on cell behavior may be mediated by changes in organelle structure and function. To test this hypothesis, human bone marrow stromal cells (hBMSCs) were cultured on poly(ϵ-caprolactone) (PCL) nanofibers scaffolds and on PCL flat spuncoat films. After 1 day-culture, hBMSCs were stained for actin, nucleus, mitochondria, and peroxisomes, and then imaged using 3D confocal microscopy. Imaging revealed that the hBMSC cell body (actin) and peroxisomal volume were reduced during culture on nanofibers. In addition, the nucleus and peroxisomes occupied a larger fraction of cell volume during culture on nanofibers than on films, suggesting enhancement of the nuclear and peroxisomal functional capacity. Organelles adopted morphologies with greater 3D-character on nanofibers, where the Z-Depth (a measure of cell thickness) was increased. Comparisons of organelle positions indicated that the nucleus, mitochondria, and peroxisomes were closer to the cell center (actin) for nanofibers, suggesting that nanofiber culture induced active organelle positioning. The smaller cell volume and more centralized organelle positioning would reduce the energy cost of inter-organelle vesicular transport during culture on nanofibers. Finally, hBMSC bioassay measurements (DNA, peroxidase, bioreductive potential, lactate, and adenosine triphosphate (ATP)) indicated that peroxidase activity may be enhanced during nanofiber culture. These results demonstrate that culture of hBMSCs on nanofibers caused changes in organelle structure and positioning, which may affect organelle functional capacity and transport.

J Biomed Mater Res Part B: Appl Biomater, 105B: 989–1001, 2017.

Key Words: bone marrow stromal cell, cell morphology, nanofiber, polymer scaffold, stem cell, stem cell niche

How to cite this article: Tutak W, Jyotsnendu G, Bajcsy P, Simon CG. 2017. Nanofiber scaffolds influence organelle structure and function in bone marrow stromal cells. J Biomed Mater Res Part B 2017:105B:989–1001.

INTRODUCTION

There has been great interest in designing tissue engineering scaffolds that can direct cell function. The physical properties of the scaffolds, namely the chemical, mechanical, and structural properties, may be appropriately designed to support cell expansion[1] or to drive stem cell differentiation.[2,3] Scaffolds have a strategic advantage as therapeutic tissue engineering devices since they are easier to fabricate, are easier to control, are more stable, have lower safety risk and have a lower regulatory burden than growth factors or stem cells.[4] Electrospun polymeric nanofiber scaffolds are of particular interest since they mimic the fibrous structure of native extracellular matrix (ECM).[5,6] Thus, fibrous scaffolds are being advanced for clinical applications, such as bladder[7] and trachea.[8]

Several reports have observed that nanofiber culture may promote osteogenic differentiation of osteoblast-like cells, embryonic stem cells, and bone marrow stromal cells.[9–14] In the case of primary human bone marrow stromal cells (hBMSCs), nanofibers drove hBMSCs into elongated, higher aspect ratio shapes with greater Z-Depth as compared to culture on flat surfaces.[13,15] Microarray testing of BMSCs demonstrated that nanofibers induced a pattern of gene expression that was similar to induction of osteogenic differentiation with biochemical supplements, and that both nanofibers and supplements lead to enrichment of genes in the Transforming Growth Factor-β pathway.[13,14,16] There is a strong link between cell shape and cell function,[17–20] and the dimensional structure of the cell niche may control cell function by influencing three-dimensional (3D) shape.[21–23] Micropatterned cell adhesive

Additional Supporting Information may be found in the online version of this article.
Correspondence to: C. G. Simon, Jr., e-mail: carl.simon@nist.gov
Contract grant sponsor: NCRR of the NIH; contract grant number: P40RR017447

surfaces were used to demonstrate that modulation of the shape of mesenchymal stem cells (MSCs) could be used to direct MSCs toward osteogenic or adipogenic differentiation.[20] Further, the cytoskeleton and the RhoA pathway were found to mediate cell-shape-directed MSC differentiation. In order to better enable the design of scaffolds that control stem cell fate, a mechanistic understanding of how scaffold structure controls cell shape and function is desirable.

Herein, we hypothesized that scaffold structure may affect cell shape, which can affect organelle structure and function, which in turn will influence overall cell behavior. Just as cells are the building blocks of organisms, organelles are the basic structural units of cells. hBMSCs were cultured on poly(ϵ-caprolactone) (PCL) nanofiber scaffolds and on flat PCL spuncoat films and then quadruple stained for actin, nucleus, mitochondria, and peroxisomes. Actin forms the cell cytoskeleton and is indicative of overall cell shape. The nucleus contains genetic material and controls gene expression. The mitochondria use food and nutrients to generate cellular energy currency while the peroxisomes metabolize fats. hBMSC organelles were imaged in 3D using confocal fluorescence microscopy and organelle 3D shapes were analyzed and compared to determine how nanofiber culture influences organelle structure.

MATERIALS AND METHODS

PCL nanofiber scaffolds

Electrospun nanofibers were made from PCL, relative molecular mass 80,000 g/mol, Sigma) with a home built electrospinning apparatus. PCL solution (10% mass fraction in 3:1 volume ratio chloroform:methanol) was loaded into a syringe and dispensed with a syringe pump at 2 mL/h in a vertical alignment with the syringe pump above the target. The positive lead from the power supply was fixed to the spinneret, which was an 18-gauge needle and the ground lead was fixed to the target (aluminum foil). The distance between needle and target was 15 cm and voltage was 16.5 kV. Tissue culture polystyrene (TCPS) disks of two diameters, 12 mm and 16 mm, were hot-punched from the bottom of TCPS dishes (100 mm dia.) and placed on the aluminum foil target. Non-woven PCL nanofiber mats were electrospun onto the TCPS disks for 1.5 h to create poly(ε-caprolactone) nanofibers (PCL-NF) samples.[13] This procedure yielded a thick layer of nanofibers that completely covered the TCPS surface so that cells seeded onto the samples would contact only PCL nanofibers and not the underlying TCPS substrate. For confocal imaging experiments, PCL-NF 16 mm dia. disks were affixed to the bottom of 24-well plates with silicon grease. For bioassays, PCL-NF 12 mm dia. disks were affixed in 48-well plates. Plates were sterilized with ethylene oxide (Anderson Products), degassed 3 days (in desiccator under house vacuum), incubated 2 days in complete medium (with serum), seeded with hBMSCs, and cultured for various times as indicated.

PCL films

PCL solutions (10% by mass in glacial acetic acid) were spin-coated (0.8 mL, 1000 rpm, 30 s) onto tissue culture polystyrene (TCPS) dishes (100 mm dia.), air-dried, annealed at 60°C for 30 s, and hot-punched into poly(ε-caprolactone) spuncoat film (PCL-SC) disks.[13] For confocal imaging experiments, PCL-SC were hot-punched from the bottoms of the dishes into 16 mm diameter disks and affixed to the bottom of 24-well plates with silicon grease. For bioassays, PCL-SC were hot-punched into 12 mm diameter disks and affixed in 48-well plates. Plates were sterilized with ethylene oxide (Anderson Products), degassed 3 days (in desiccator under house vacuum), incubated 2 days in complete medium (with serum), seeded with hBMSCs, and cultured for various times as indicated.

Scanning electron microscopy (SEM) and atomic force microscopy (AFM)

PCL nanofibers and spuncoat films were imaged by scanning electron microscopy (SEM). Samples were sputter-coated with thin layer of gold (Denton Vacuum Desk II, 15 kV, 80 s) prior to imaging (Hitachi S-4700-II FE-SEM, 5 kV, WD= 12 cm). Nanofiber diameters were determined by analyzing electron micrographs using ImageJ software (NIH). All nanofiber and film samples for the study were made in one batch. For determining nanofiber diameter, two nanofiber samples were randomly chosen and three evenly spaced SEM images were collected on each sample. SEM Images were analyzed and the mean nanofiber diameter was found to be 325 nm (standard deviation (S.D.) = 256 nm, $n = 60$ fibers).

Surface roughness of the spuncoat films was measured using atomic force microscopy (AFM, Dimension Icon, Bruker, Billerica, MA). Three film samples were analyzed with three spots per sample for a total of nine spots measured. The spot size was 50 μm × 50 μm, the scans were acquired with 256 samples per line, and images were analyzed with Nanoscope Analysis (Bruker). The root mean square (RMS) roughness was determined for each analyzed spot and the mean RMS roughness was 92.8 nm (S.D. = 10.7 nm, $n = 9$).

Cell culture

Primary human bone marrow stromal cells (hBMSCs) were obtained from the Texas A&M Health Science Center (donor #8001R, female, 24 years). These cells have been characterized according to the criteria for "mesenchymal stem cells" described in Dominici et al.,[24] including measurements of morphology, colony forming units, surface markers (flow cytometry), and *in vitro* differentiation tests (bone and fat). hBMSCs were cultured at 37°C under 5% by volume CO_2 in α-minimum essential media (Invitrogen) containing 16.5% by volume fetal bovine serum (FBS, Atlanta Biologicals), 4 mmol/L L-glutamine (Invitrogen), and penicillin/streptomycin (100 U/mL penicillin and 100 μg/mL streptomycin, Cellgro).[13] hBMSCs were trypsinized (0.25% by mass containing 1 mmol/L ethylenediaminetetraacetate (EDTA), Invitrogen) at 70% confluency and seeded onto the various substrates. Passage 4 hBMSCs were used for all experiments. For confocal imaging experiments, experiments were conducted in 24-well plates with 1 mL of medium per well with 15,000 cells seeded per well. For bioassays, experiments were conducted in 48-well plates with 0.5 mL of medium per well and 20,000 cells per well.

Staining organelles in hBMSCs

hBMSCs were seeded on substrates, cultured 24 h in medium with serum, and medium was removed. Serum-free medium

TABLE I. Labels Used to Stain Organelles

Organelle	Labels	Dye excitation maximum (nm)	Laser line used to excite	Dye emission maximum (nm)	Emission wavelength range collected
Mitochondria	Mitotracker CMXRos	579	633	599	590–619
F-Actin	Alexa Fluor-546 Phalloidin	545	543	570	558–585
Peroxisomes	Peroxisome-GFP	475	476	525	515–545
Nucleus	DAPI	358	405	461	435–480

containing 350 nmol/L Mitotracker Red CMXRos (1H,5H, 11H,15H-Xantheno[2,3,4-ij:5,6,7-i'j']diquinolizin-18-ium, 9-[4-(chloromethyl)phenyl]-2,3,6,7,12,13,16,17-octahydro-, chloride, Invitrogen, M7512) was added.[25,26] MitoTracker Red CMXRos accumulates in mitochondria of live cells through a charge-based interaction and remains after cell fixation (Table I).[26] Plates were incubated for 1.5 h in the cell culture incubator, washed with phosphate buffered saline (PBS), and replenished with fresh serum-free medium. CellLight Peroxisome-green fluorescent protein (GFP) was added to each well (6 μL/well, Invitrogen) and plates were incubated for 16 h in the cell incubator. CellLight Peroxisome-GFP uses an insect cell vector (baculovirus) to transfect the hBMSCs with green fluorescent protein (GFP) that is coupled to a peptide (serine-lysine-leucine, peroxisome targeting signal) that targets the GFP to the peroxisomes.[27] The peroxisome-GFP transgene is controlled by a mammalian promoter that is recognized by the hBMSCs while the viral genes and their promoters are not. After 16 h incubation, samples were washed in PBS, fixed in 3.7% formaldehyde (volume/volume in PBS) for 0.5 h, washed with PBS, and permeabilized with 0.2% by mass Triton X-100 for 5 min. The samples were stained with Alexa Fluor 546-phalloidin (F-actin stain, 20 nmol/L in PBS, Invitrogen)[28] and DAPI (4',6-diamindo-2-phenylindole, dihydrochloride, 300 nmol/L in PBS, Invitrogen).[26] Finally, samples were washed in the PBS, washed in water, and air dried.

Confocal microscopy

Images were collected using a Leica TCS SP5 II laser-scanning confocal microscope. An oil-immersion 63×/1.42 numerical aperture objective was used to collect z-stack images (approximately 50 z-sections collected at 126 nm spacing for each cell, 1024 × 512 pixels, 8 bit tiff images) for nuclei, mitochondria, peroxisomes, and F-actin. Images were acquired by setting the pinhole to between 1 to 2 airy units, x–y–z voxel dimensions of 123 nm × 123 nm × 126 nm, digital magnification of 1× to 2×, and line averaging of $n = 3$. The images were obtained using sequential acquisition setup to prevent bleed-through from the four fluorescent dyes. Fifteen single cells (not touching or overlapping with other cells) were randomly selected for the image analysis. Distances in all images were assigned using an optical micrometer.

Organelle image analysis

Organelle area, perimeter, and aspect ratio. For determining organelle area, perimeter, and aspect ratio, a z-projection based on maximum intensity was created (x–y view) in ImageJ[29] and the z-projection was thresholded (from selecting "dark background" in ImageJ). A region of interest was manually drawn around each organelle using "ROI Manager" and the shape metrics were determined. All segmented organelles are shown in Supporting Information Figure S1.

Z-Depth. For Z-Depth, each z-stack was rotated 90° on the y-axis using the ImageJ "3D Project" function, a maximum intensity projection of the z–y view was created each image was manually thresholded to maximize the cell pixel selection but minimizing pixel selection outside the cell. The maximum thickness of the organelle along the z-axis in the z–y view was measured in ImageJ using the image ruler (defined herein as "Z-Depth").

Organelle volume and surface area. Organelle volume and surface area were calculated in ImageJ using the "3D Convex Hull" plug-in. The organelles were manually thresholded in ImageJ and a "region of interest" surrounding the organelles was selected to minimize background contributions. The "3D Convex Hull" plugin calculates the convex hull of the selected organelle in the image sequence uses the convex hull to determine volume and surface area.

Centre of mass and distances between organelles. The "Object Counter3D" Image J plug-in was used to calculate center of mass of the organelles.[30] The organelles were manually thresholded in ImageJ and a "region of interest" surrounding the organelles was selected to minimize background contributions. The plugin determines the center of mass in x, y, and z coordinates. The distances between the organelle Centers of Mass were determined from the x, y, and z coordinate positions (in physical dimensions) of each organelle using the following equation based on the Pythagorean theorem: Distance from "Organelle a" (x_a,y_a,z_a) to "Organelle b" $(x_b,y_b,z_b) = \mathrm{sqrt}[(x_a-x_b)^2 + (y_a-y_b)^2 + (z_a-z_b)^2]$.

Generating a 3D representation of organelle positions

Although the mean distances between the organelles was determined by image analysis, the mean positions of the organelles cannot be plotted in 3D without generating mean x–y–z coordinates for each organelle. The mean inter-organelle distances were converted into x–y–z coordinates using a multidimensional scaling application in Matlab (MATLAB and Statistics Toolbox Release 2012b, The MathWorks, Inc.). Next, the x–y–z coordinates for organelles from nanofibers and films were aligned qualitatively in 3D coordinate space using a Procrustes solution to minimize the distance between the paired organelles: distances between "actin-nanofibers" and "actin-films", "nucleus-nanofibers" and "nucleus-films", "mitochondria-

nanofibers" and "mitochondria-films", and "peroxisomes-nanofibers" and "peroxisomes-films" were minimized. Procrustes determines a linear transformation (translation, reflection, orthogonal rotation, and scaling) of the 3D points for the films to best conform them to the 3D points for the nanofibers. A Matlab Procrustes implementation was used and "the scaling in the linear transformation estimation" was disabled.

Bioassays

Overview. Five bioassays (Picogreen DNA, peroxidase, adenosine triphosphate (ATP), WST-1 bioreductive potential, and lactate) were conducted to assess differences in metabolic activity for hBMSCs cultured on nanofibers versus films. Four replicates were run for each treatment at each time point. Each assay was run twice using separate cell cultures. Negative controls for background were subtracted from all data for all assays. Negative controls were substrates (nanofibers or films) that were incubated in full culture medium for 1 day, 14 days, 21 days or 28 days without hBMSCs but with full medium changes, and then assayed in the exact same manner as substrates with hBMSCs.

Picogreen DNA assay. Total DNA content for each scaffold was determined using the Picogreen assay (Invitrogen).[31] After the indicated cell culture times (1 day, 14 days, 21 days, and 28 days), the scaffolds with adherent hBMSCs were rinsed in PBS and incubated in 1 mL of digestion buffer (PBS with 0.175 U/mL papain and 14.5 mmol/L L-cysteine) for 17 h at 60°C. An aliquot (100 μL) of lysate was transferred to a 96-well plate and mixed with 100 μL of Picogreen working reagent according to manufacturer's instructions. Fluorescence (excitation 485 nm, emission 538 nm) was measured using a plate reader (Molecular Devices, SpectraMax M5). DNA concentration was determined by making a standard curve from known DNA concentrations.

Peroxidase assay. Quantitative assessment of peroxisome activity was carried out by using Amplex Red Hydrogen Peroxide/Peroxidase Assay according to manufacturer's instructions (Invitrogen). In the presence of peroxidase, Amplex Red reagent (10-acetyl-3,7-dihydroxyphenoxazine) reacts with hydrogen peroxide to produce red fluorescent resorufin.[32] Samples were rinsed with PBS, 0.25 mL of PBS was added to each well, and cells were scraped off the samples using a rubber policeman into the PBS. The scraped cell suspensions were transferred to 1.5 mL vials and sonicated over ice (Sonics, Vibra Cell, 30 sec at 30% power) to release peroxisomes. An aliquot (0.1 mL) of the lysate was mixed with 0.1 mL of Amplex Red working solution (100 μmol/L Amplex Red and 2 mmol/L hydrogen peroxide) in a 96-well plate. Fluorescence measurements were taken every 5 min for 30 min using a platereader (571 nm excitation, 585 nm emission). Peroxidase activity was determined using controls of a known amount of horseradish peroxidase standard provided with the kit. Additional "sonication" controls were run to insure that sonication did not degrade the peroxidase activity; horseradish peroxidase enzyme (provided in the kit) in PBS was sonicated and its activity did not degrade.

ATP assay. Intracellular ATP (adenosine triphosphate) levels were evaluated using a Bioluminescent Somatic Cell Assay Kit following manufacturer's protocols (Sigma-Aldrich). Luciferase converts luciferin to adenyl-luciferin in the presence of ATP and this reaction releases light.[33] In a dark room, substrates with hBMSCs were rinsed in PBS and transferred to a clean 48-well plate containing 150 μL of Somatic Cell Releasing Reagent (formulation provided with the kit containing EDTA and Triton X-100 (p-tertiary-octylphenoxy polyethyl alcohol)) in each well. Plates were gently swirled for 8 min and 0.1 mL of the lysate was transferred to a 96-well plate containing 0.1 mL of ATP Assay Mix in each well. Luminescence was measured immediately using a platereader at 570 nm for 15 min at 5 min intervals. ATP concentration was determined using controls of a known amount of ATP standard as provided by the manufacturer.

WST-1 assay. A colorimetric WST-1 (2-(4-iodophenyl)-3-(4-nitrophenyl)-5-(2,4-disulfophenyl)-2H-tetrazolium, monosodium salt) assay kit was used to measure the bioreductive potential of cells (NADH-driven, nicotinamide adenine dinucleotide) according to manufacturer's instructions (Dojindo, Gaithersburg, MD).[34] hBMSCs on PCL-NF or PCL-SC were rinsed in PBS and 0.55 mL WST-1 solution was added to each well (PBS containing 45 mmol/L of WST-1 and 2 mmol/L of 1-methoxy-5-methylphenazinium methylsulfate). After incubating the plate for 2 h at 37°C, 0.2 mL was transferred from each well to a clean 96-well plate for absorbance measurements at 450 nm using a platereader. Measurements were background subtracted using controls.

Lactate assay. Lactate concentrations in culture medium were measured with an enzymatic assay (Trinity Biotech, Abingdon, UK) according to manufacturer's instructions. In the assay, lactate oxidase converts lactic acid to pyruvate and hydrogen peroxide.[35] Peroxidase is also present in the reaction solution, which uses the hydrogen peroxide to catalyze the oxidation of chromogen precursors, which absorb at 540 nm. After the indicated cell culture times, medium in each well was replaced with fresh medium and incubated for 8 h. An aliquot (0.01 mL) of the culture medium was transferred to a clean 48-well plate and mixed with 0.3 mL of lactate reaction solution (prepared according to manufacturer's instructions). After incubation for 10 min at room temperature, absorbance at 540 nm was measured using a platereader. Lactate concentration was determined by making a standard curve from lactate standards supplied by manufacturer.

RESULTS

Cell and organelle morphology

The morphology of electrospun PCL nanofiber scaffolds and spuncoat PCL films are shown in scanning electron micrographs in Figure 1, examples of quadruple stained hBMSCs are shown in Figure 2, and plots of organelle shape metrics are in Figure 3. Measurements of actin are used as cell volume measurements since actin defines all of the intracellular space. The area, perimeter, and volume of all organelles (actin, nucleus, mitochondria, and peroxisomes) were

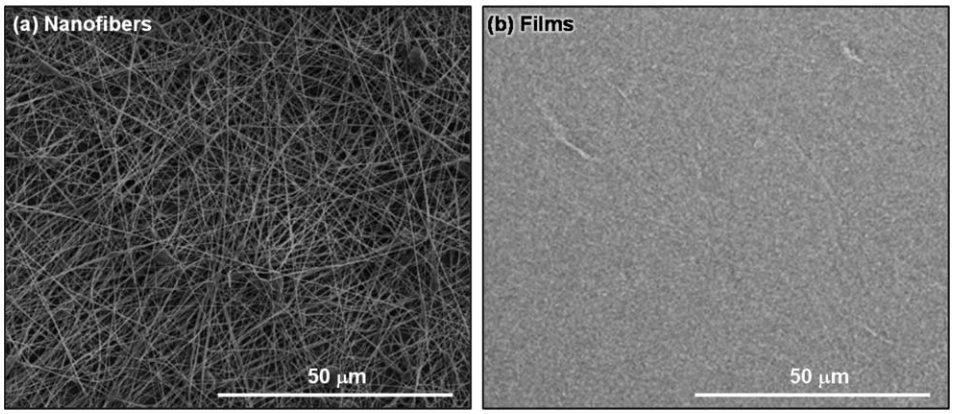

FIGURE 1. Scanning electron micrographs (SEM) of (a) electrospun PCL nanofiber scaffolds and (b) PCL flat films.

smaller during culture on nanofibers than on films [Figure 3(a,b,d)]. hBMSCs and their organelles had a more elongated shape (aspect ratio) and greater 3D character (Z-Depth) during culture on nanofibers [Figure 3(c,f)]. There were no significant differences in cell surface area between films and nanofibers [Figure 3(e)]. These results demonstrate that effects of the culture environment on cell shape can affect organelle shape.

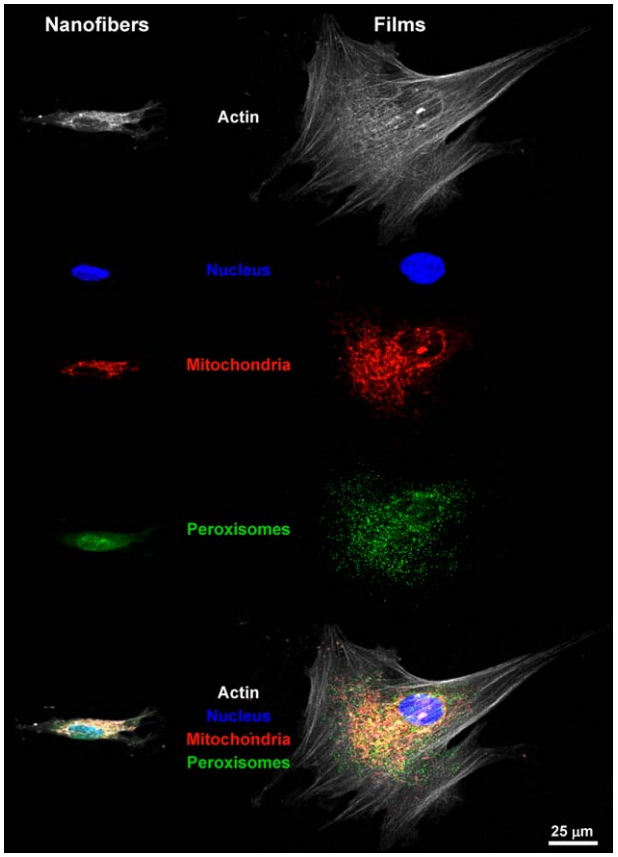

FIGURE 2. Images (x-y view) of representative hBMSCs from electrospun PCL nanofibers and PCL films. Images from each of the four organelle stains are shown as well as a combined image of all four labels.

In order to determine if the cell volume fraction occupied by the organelles changes between nanofibers and films, the ratios of organelle area, volume, and surface areas were plotted in Figure 4. The nucleus, mitochondria, and peroxisomes occupy a significantly ($p < 0.05$) larger fraction of hBMSC area ("Nucleus/Actin", "Mitochondria/Actin", and "Peroxisomes/Actin") during culture on nanofibers than on films [Figure 4(a)]. In addition, the nucleus and peroxisomes occupy a significantly ($p < 0.05$) larger fraction of hBMSC volume ("Nucleus/Actin" and "Peroxisomes/Actin") during culture on nanofibers than on films [Figure 4(b)]. These differences are depicted in Figure 5 using circles (area) and spheres (volume) drawn to scale, to more visually demonstrate the larger volume fraction occupied by nucleus and peroxisomes during nanofiber culture [Figure 5(b)].

Organelle positioning

The geometrical centers of each organelle were used to determine 3D inter-organelle distances [Figure 6(a)]. The distances between all organelles were smaller during culture on nanofibers as compared to films, and all but one (mitochondria to peroxisome) of these differences were significant ($p < 0.05$). Since the volume of hBMSCs (actin volume) was 4.1-times smaller on nanofibers than on films [Figure 3(d)], ratios of the inter-organelle differences were calculated to determine if the inter-organelle distances were scaling proportionally with volume changes [Figure 6(b)].

If the organelle volumes are modelled as spheres, then geometric principles indicate that a 76% decrease in cell actin volume when going from films to nanofibers will correspond to a 37% decrease in sphere radius (calculations in Supporting Information Figure S2). If the inter-organelle distances are scaling proportionally with changes in hBMSC volume, then inter-organelle distances on nanofibers should be 37% lower than films (nanofiber/film inter-organelle distance ratio = 0.63). Figure 6(b) shows that the nanofiber/film inter-organelle distance ratios for "nucleus to peroxisome" (0.62) and "mitochondria to peroxisome" (0.70) scaled nearly proportionally with hBMSC volume changes, but that the other four inter-organelle distances did not. The nanofiber/film distances ratios from "actin to nucleus" (0.46), "actin to mitochondria" (0.39), "actin to peroxisome"

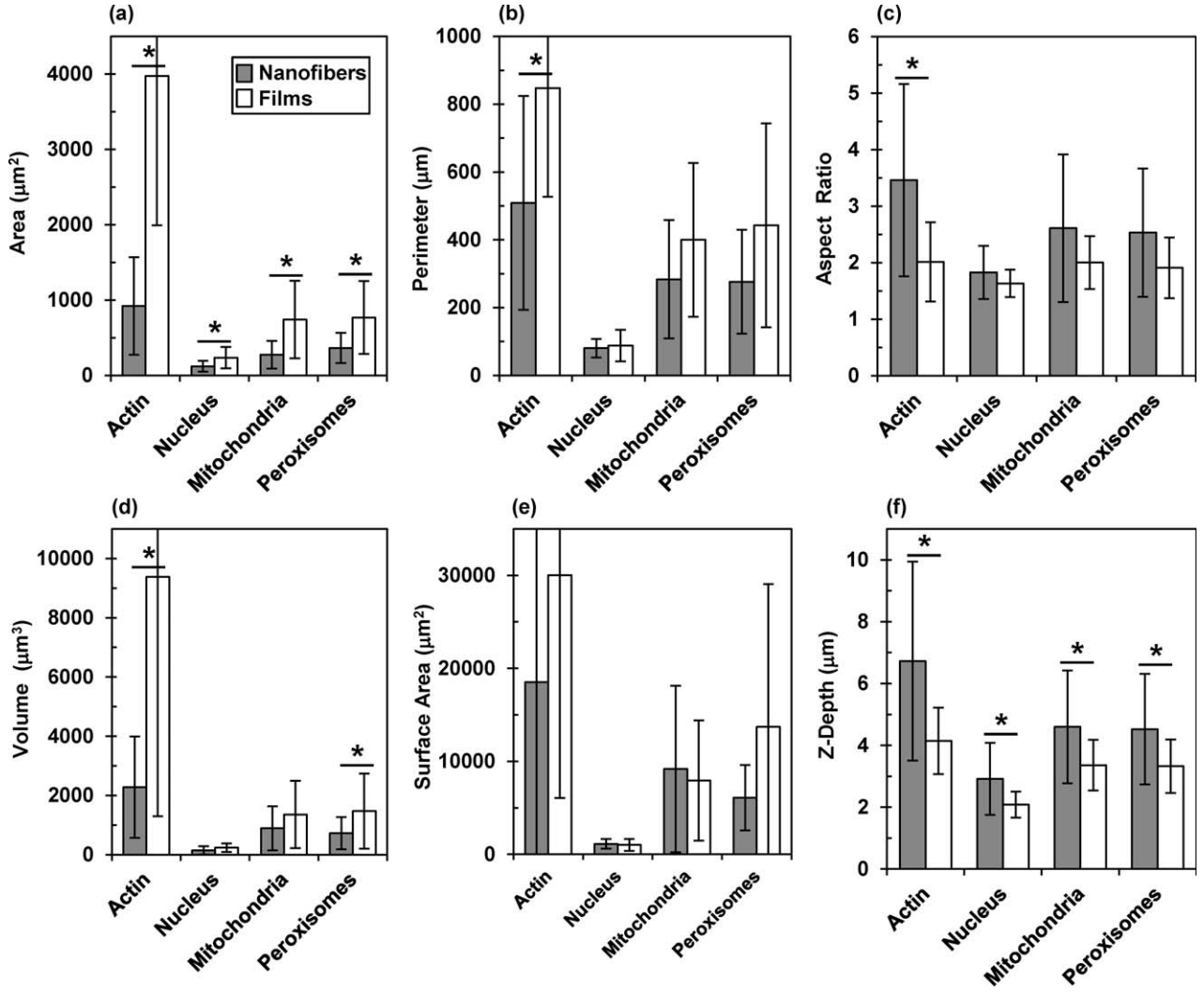

FIGURE 3. Shape metrics of hBMSCs cultured 1 day on PCL nanofibers or PCL films. All data are means and error bars are standard deviation ($n = 15$). Asterisks indicate significant differences (t test, $p < 0.05$).

(0.42), and "nucleus to mitochondria" (0.51) were smaller than would be expected if the inter-organelle distances were scaling with volume change. These results suggest that hBMSCs may actively position their organelles in response to the properties of their microenvironment, and that they actively positioned the nucleus, mitochondria and peroxisomes closer to the geometrical center of the cell (actin) during culture on nanofibers.

Multidimensional Scaling

In order to enable a 3D visual comparison of organelle positions, multidimensional scaling was used to translate the inter-organelle distances into x–y–z coordinates and a Procrustes solution was used to align the organelles from nanofibers and films in 3D. Plots of the aligned organelle coordinates are shown from three perspectives (XY, ZY, and XZ) in Figure 7(a,b) shows a 3D rendering of the organelle positions. These plots show graphically how the organelles are more tightly grouped in hBMSCs cultured on nanofibers. The ZY and XZ plots in Figure 7(a) show that the larger inter-organelle distances for films are achieved by movements in the XY plane and not by extending in the z-direction. The range of the organelle positions along the z-axis is higher for nanofibers (2.3 μm) than for films (1.7 μm). These results correlate with Figure 3(f), where Z-Depth of the organelles was larger for hBMSCs on nanofibers, and further support the notion that hBMSC organelle morphologies have greater 3D character on nanofiber scaffolds.

Due to the challenge of collecting confocal z-stacks, the current work assessed 15 cells in each scaffold (15 cells × two treatments (NF and SC) × four organelles = 120 z-stacks). The reliability of this sample size was assessed by randomly splitting the data sets into two groups (one of eight cells and one of seven cells), re-calculating the means for the shape metrics, and then comparing to the means from 15 cells. When this was done for the seven organelle shape metrics present in Figures 3 and 7, the means of the two random groupings differed by an average of 14% from the original set of 15.

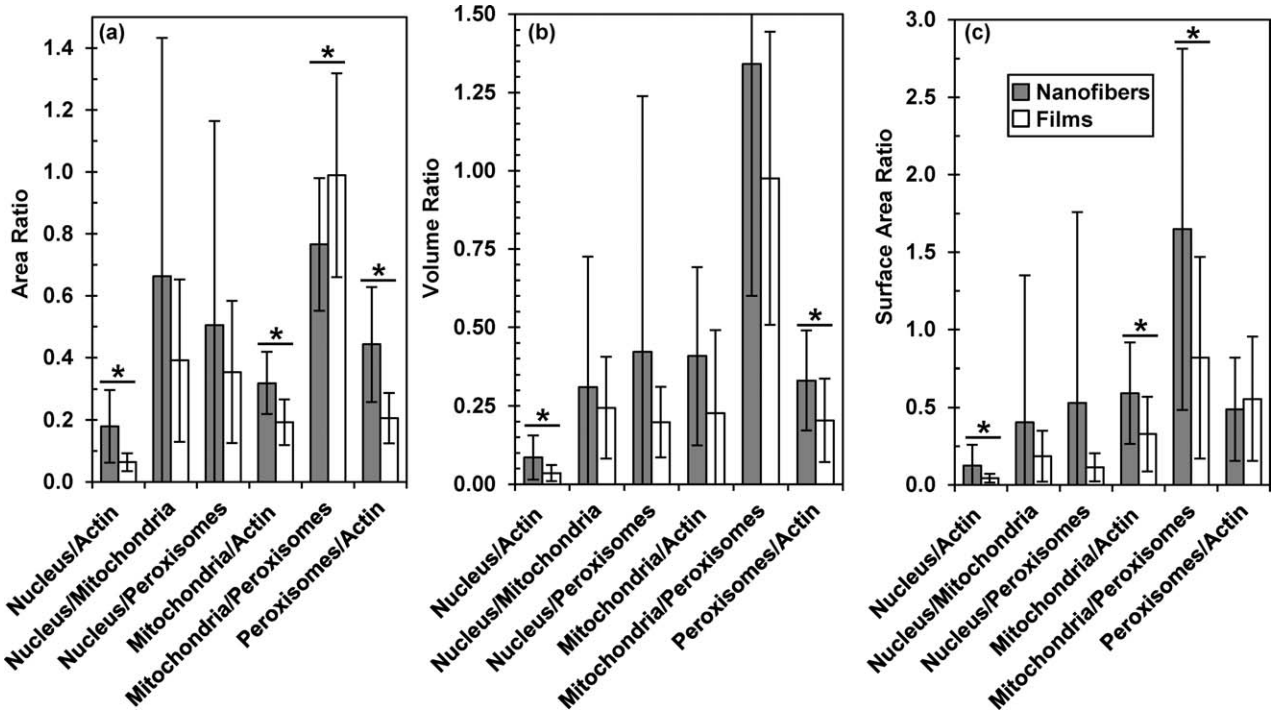

FIGURE 4. Ratios of organelle area, volume and surface area were calculated. All data are means and error bars are standard deviation ($n = 15$). Asterisks indicate significant differences (t test, $p < 0.05$).

Bioassays for organelle function

To determine if nanofiber-induced changes in actin, nuclear, mitochondrial, and peroxisomal shapes caused changes in organelle functions, five bioassay measurements were made: DNA concentration (Picogreen), peroxidase activity, WST-1 bioreductive potential, ATP concentration, and lactate

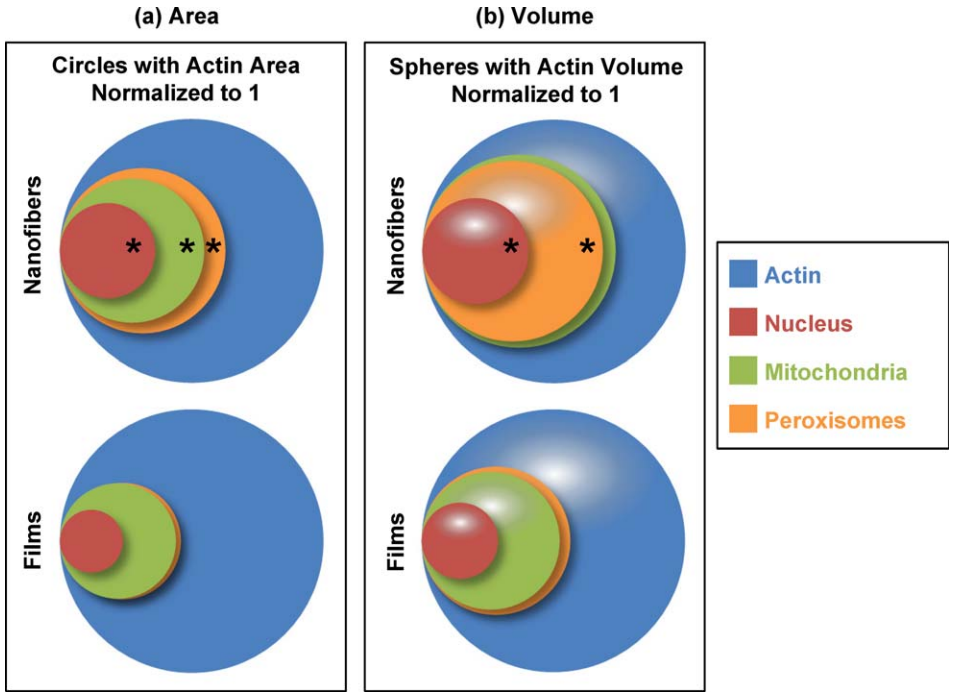

FIGURE 5. Diagram to visualize differences in organelle area and volume fractions. The circles and spheres represent the organelles, are drawn to scale using the data in Figure 4(a,b) and are color-coded according to the legend. (a) The circles represent organelle area. Actin area (blue circles) was normalized between nanofibers and films. (b) The spheres represent organelle volume. The actin volume was normalized between nanofibers and films. Asterisks indicate organelles that occupy a significantly larger actin area-fraction or actin volume-fraction in nanofibers than in films (t test, $p < 0.05$).

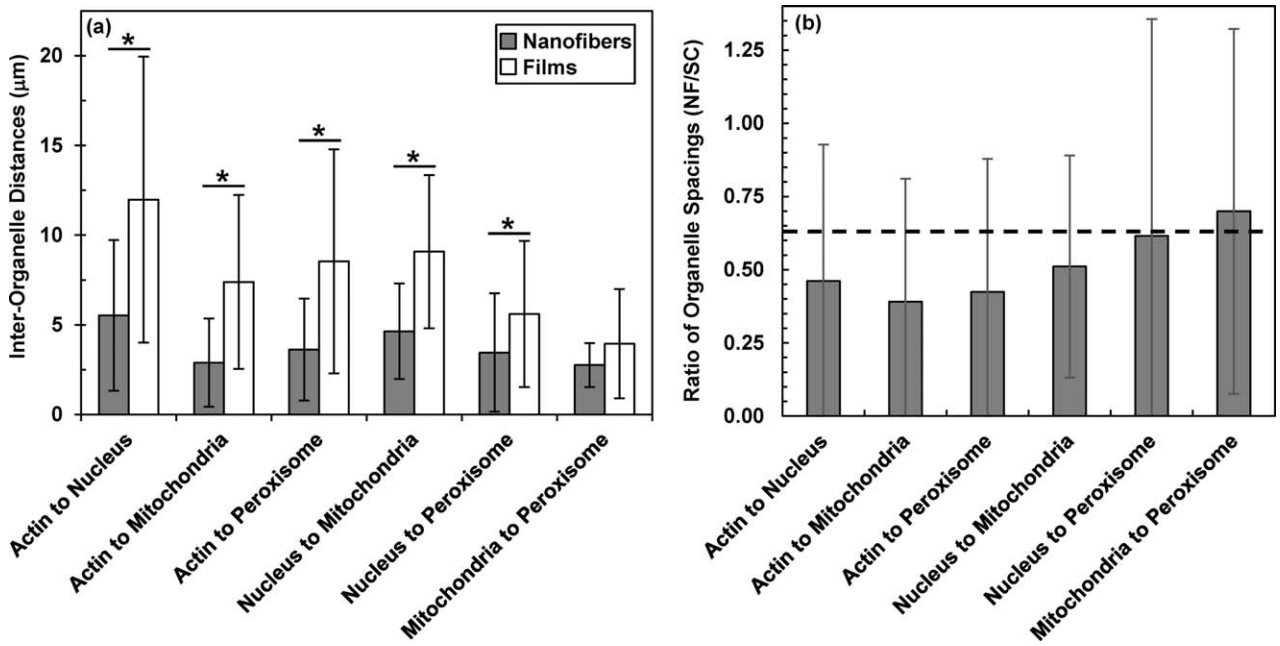

FIGURE 6. (a) Plot of inter-organelle distances. All data are means and error bars are standard deviation ($n = 15$). Asterisks indicate significant differences (t test, $p < 0.05$). (b) Inter-organelle distance ratios for nanofiber divided by film. The error bars were derived by propagating the standard deviations from panel (a) $[\delta(NF/SC) = |NF/SC| * [(\delta NF/NF)^2 + (\delta SC/SC)^2]^{1/2}]$. The dotted line at 0.63 is the ratio expected if the organelle positions are scaling linearly with differences in hBMSC volume on nanofibers and films.

concentration (Figure 8). Picogreen DNA assay showed that hBMSCs proliferated from 1 day to 14 days, reaching a plateau that was essentially sustained from 14 days through 21 days and 28 days. There were no consistent significant differences between nanofibers and films for DNA, WST-1, ATP, or lactate measurements. However, hBMSCs had higher peroxidase activity on nanofibers at all four time points and these differences were significant ($p < 0.05$) for three of the four time points (1 day, 21 days, and 28 days). These results suggest that culture of hBMSCs on nanofibers may affect metabolism involving peroxisomes and peroxidases.

DISCUSSION

Weiss and Garber first observed in 1952 that the fibrous structure of fibrin microenvironments caused mesenchymal cells to take on elongated morphologies that influenced their migration and they realized that it was important to "determine the physical basis, the mechanism, underlying this correlation."[36] In the current work, the mechanisms of how nanofiber scaffolds may enhance osteogenic differentiation were investigated by examining the 3D morphology of cell organelles. Culture on nanofiber scaffolds influenced the hBMSC actin structure and the structure of organelles: nucleus, mitochondria, and peroxisomes. Differences in organelle Z-Depth, area, aspect ratio, and volume were observed and these results support previous measurements of hBMSC actin morphology.[13,15]

Although the peroxisomes had a smaller volume during culture on nanofibers, the peroxisomes occupied a larger cell volume fraction, suggesting that the peroxisomal functional output may be enhanced during nanofiber culture. This result was supported by the peroxidase bioassay, which showed that hBMSCs had greater peroxidase activity during nanofiber culture. In addition, the inter-organelle distances were reduced during nanofiber culture. These distance reductions were greater than predicted by scaling in proportion to the cell volume reduction on nanofibers, suggesting that active mechanisms may be used to reposition organelles to a more cell-centric position during nanofiber culture. The smaller hBMSC volume and more centralized organelle positioning would reduce the energy cost of inter-organelle vesicular transport during culture on nanofibers (Figure 9).

There is a strong connection between nuclear shape and cell function,[37,38] and cell substrates that influence cell shape can also influence nuclear shape.[39–41] For mouse osteocytes, Himeno-Ando et al. observed *in situ* a larger nucleus/cell volume ratio in tibial bones as compared to parietal bones,[42] which suggests that there may be different functional or microenvironmental demands placed on the osteoblasts in these bones. A number of mechanisms for how changes to cell and nuclear shape may lead to changes in cell function and gene expression are being advanced. One mechanism is a contiguous physical connection between the ECM and the nuclear genome: a direct link from the ECM to cell surface receptors to the cytoskeleton to the nuclear matrix to DNA.[43] The nuclear matrix, also called a nucleoskeleton, is a proteinaceous matrix that provides structure to the nucleus and interacts with chromatin and DNA to participate in the physical regulation of gene expression. By this mechanism, changes to cell shape may directly cause conformational changes in the promoter regions of genes that enable transcription factor binding

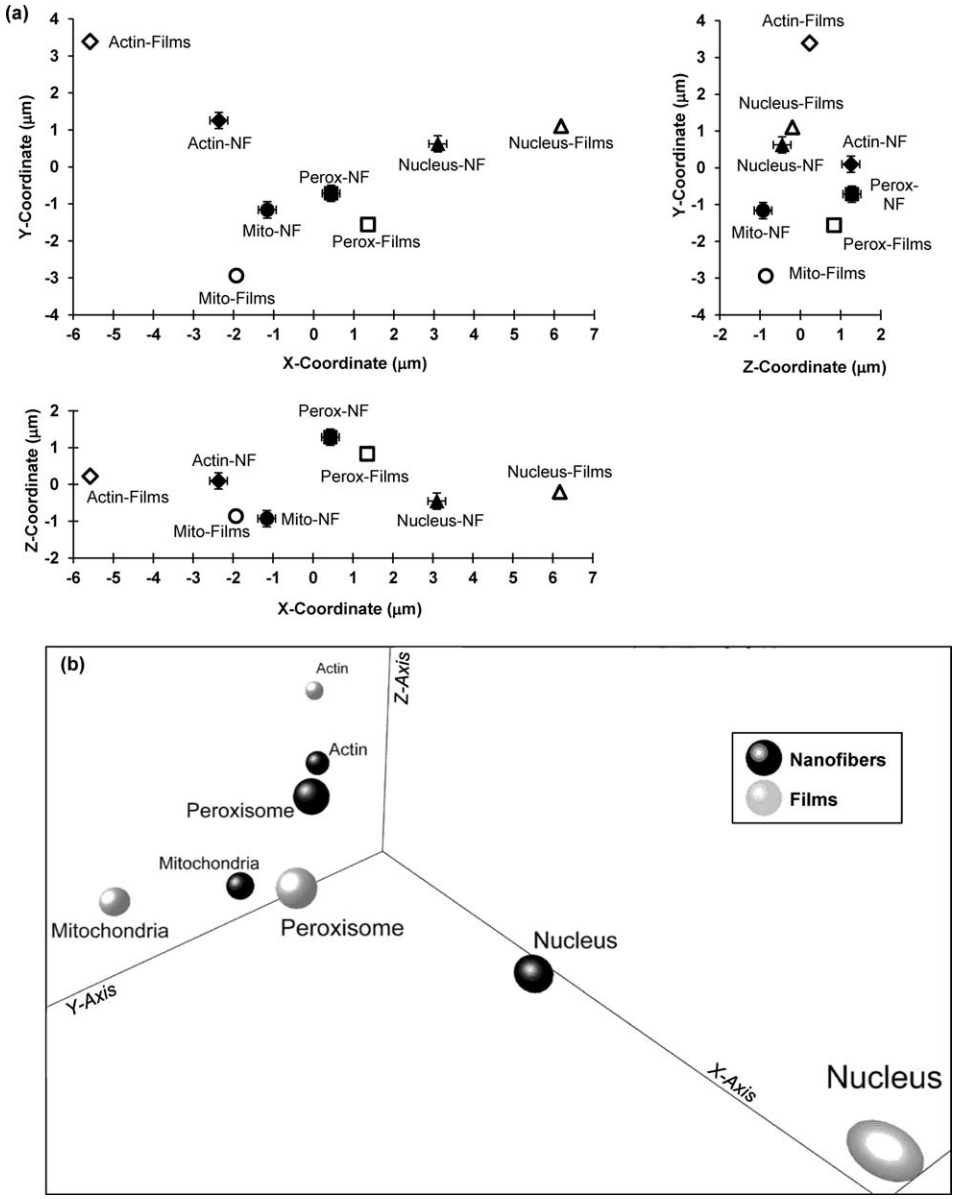

FIGURE 7. The inter-organelle distance data in Figure 6 was used to generate mean x–y–z coordinates for the organelles using multidimensional scaling. The goodness of fit of the resulting x–y–z coordinates points was 0.22 μm for nanofibers and 0.049 μm for films (using the maximum of normalized absolute differences between input and estimated distance matrix entries). These values represent the largest inter-organelle distances errors after the multidimensional scaling and were used for the error bars in panel (a). Note that the error bars for the films (0.049) are too small to see in the figure. A Procrustes solution was used to qualitatively align the x–y–z coordinates for organelles for nanofibers and films so they could be displayed and compared in the same plot. (a) The aligned positions of the organelles are shown (a) in three 2D-plots from three perspectives (XY, ZY, and XZ) and (b) in a 3D plot. (b) Error bars were omitted for clarity, but are the same as in Panel (a).

and gene expression.[40,43,44] This concept is especially relevant to osteogenic differentiation, since the most well-known osteogenic transcription factor, RUNX2 (CBFA1), which binds to the osteocalcin promoter, was identified as a nuclear matrix protein (NMP-2).[45] RUNX2 is considered an architectural transcription factor, which binds to DNA and causes it to bend to physically bring promoter elements into closer proximity.

The morphology of biological systems is determined by scaling laws that balance the functional requirements of fitness and survival with physical properties such as volume, surface area, enzyme activity, transport, heat transfer, reactant concentrations, and the microenvironment.[46–48] A striking example of this is the 20-year bacterial evolution experiment where E. coli (Escherichia coli) were cultured *in vitro* for 40,000 generations.[49] The E. coli increased their volume and some strains lost their characteristic rod-like morphology and evolved a spherical shape, which reduced their surface area to volume ratio and improved their fitness for the culture microenvironment.[50] A sphere has the lowest surface area to volume ratio for a given volume and elongated, high aspect ratio cells will have greater surface area

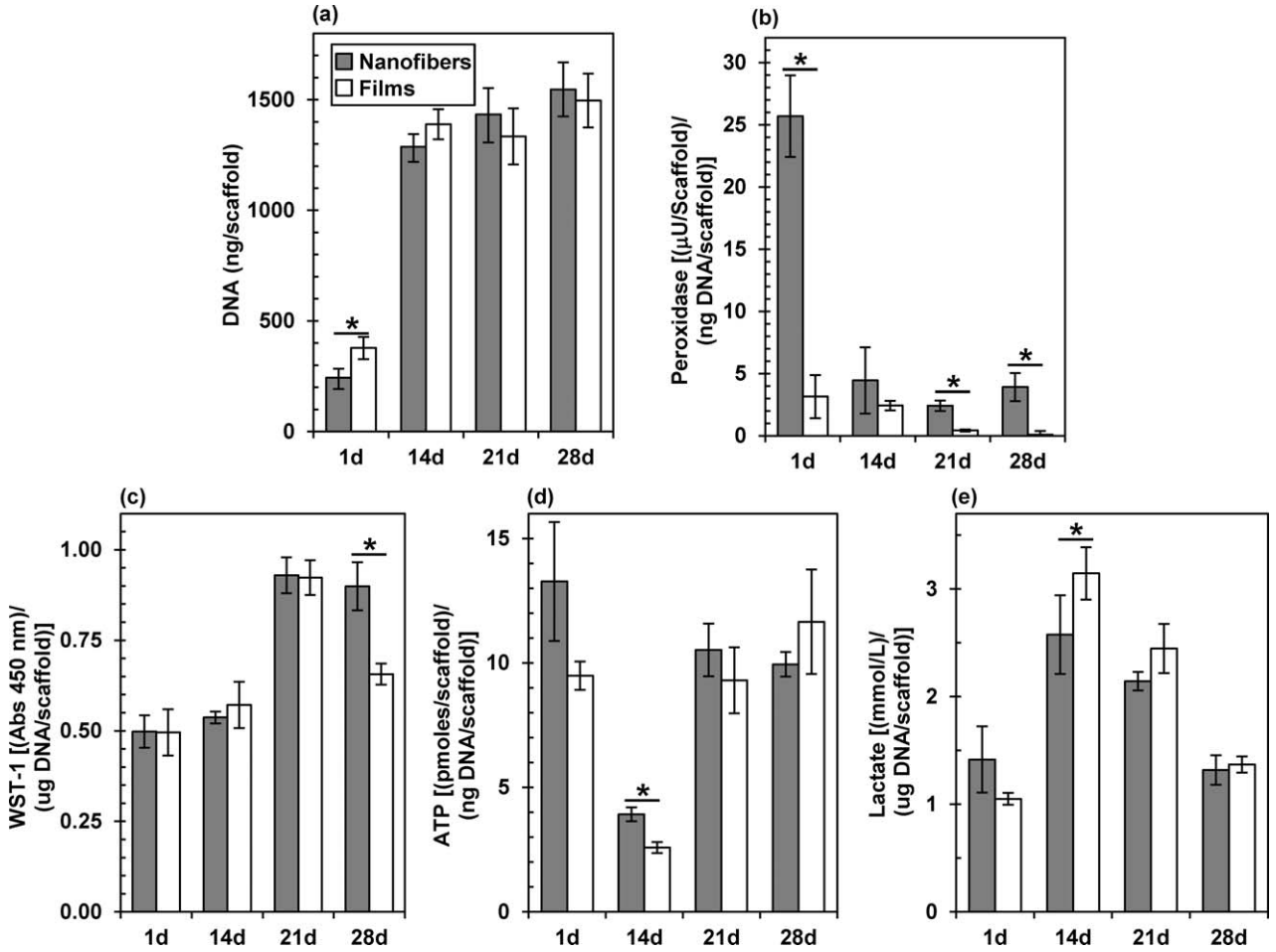

FIGURE 8. Assays to assess differences in metabolic activity of hBMSCs cultured on nanofibers or films. All data are means and error bars are standard deviation ($n = 4$). Asterisks indicate significant differences (t test, $p < 0.05$) between nanofibers and films.

for receiving or emitting solutes.[47] Enlightening *in vitro* data come from experiments where the interconnections between lipid vesicles loaded with various enzyme/substrate combinations were manipulated.[51] Changing the network topology from linear to circular drastically affected the reaction kinetics and demonstrate how changes in organelle structure may affect cell function.

Organelle structure is linked to functional capacity[48] and, for example, larger mitochondrial volume and surface area correlate with higher mitochondrial enzyme activity.[52] A change in volume will change the concentration of reactants and reaction rates.[51] Herein, the 76% decrease in cell volume on nanofibers (compared to flat films) may be expected to cause a 4.1-fold increase in concentration in intracellular molecules. Cells regulate the amount of their lipid membrane, where exocytosis, endocytosis, and membrane folding/unfolding are used to increase or decrease cell/organelle volume.[53,54] Organelle shape also affects intracellular transport and signal transduction cascades. Diffusion of molecules from a centrally located organelle reaches the entire cell volume more quickly than molecules diffusing from the far end of an elongated cell.[48] An organelle that is compact will sample less cell volume than an organelle that is widely distributed, which will influence how quickly cargo can be delivered from the organelle to its destination. Modelling of signal transduction cascades indicates that membrane-bound second messenger concentrations are decreased at the tips of elongated cells when the signal originates from the cytoplasm, leading to molecular signaling gradients.[55] Models of G-protein-coupled receptors indicate that deactivation of the second messengers can depend on cell/organelle shape, whereby membrane-originating signals may fully penetrate the cytoplasm of flat cells but be unable to reach the center of spherical cells.[56] Thus, physical mechanisms link cell/organelle structure with cell function.

Cellular metabolism is also linked to cell function and behavior. Warburg first described how cancer cells switch from oxidative metabolism to less efficient glycolytic metabolism,[57] which may provide the proper secondary metabolites to support the anabolism of the molecules required for cell proliferation.[58] In addition, glycolysis requires less oxygen, which may help cancer cells accommodate the hypoxic tumor environment.[59] Glycolysis may also be faster at providing the ATP required for proliferation than oxidative phosphorylation.[58] Likewise, differentiation of embryonic stem cells involves a change from glycolysis to oxidative

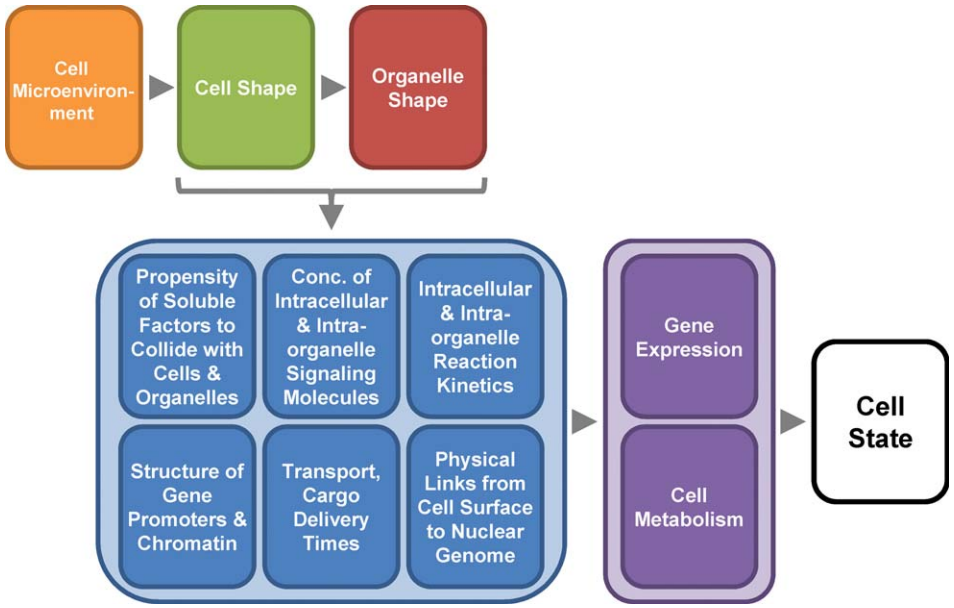

FIGURE 9. Model for inter-relationship between cell microenvironment, cell and organelle shape and cell state. Microenvironmental cellular cues (orange), such as scaffold structure, can influence cell shape (green). Cell shape, in turn, can affect the shape of organelles (maroon). These changes in cell and organelle shape lead to physical effects on the cellular components (blue), such as (i) changes in likelihood that a soluble factor will collide with the organelle, (ii) changes in concentrations of intracellular and intraorganelle signaling molecules, (iii) changes in reaction kinetics (diffusion times), (iv) changes in structure of gene promoters and chromatin, (v) changes in cargo delivery times via molecular motors and (vi) changes in the structure of the physical link between the extracellular matrix (ECM) and the nuclear genome. Physical effects on cellular components can influence cell metabolism and gene expression (purple), which may dictate cell states (white), such as cell function, differentiation or proliferation.

phosphorylation and an increase in mitochondria, which are responsible for oxidative metabolism.[60] Reprogramming of somatic cells into "induced pluripotent stem cells" (iPSCs) is accompanied by a reduction in mitochondria and a switch to glycolysis.[61] Thus, changes in cell function and differentiation are coupled to changes in cell metabolism.

Osteogenic differentiation may also be concomitant with a shift to oxidative phosphorylation,[62] despite the high energy demands of fabricating a bony, mineralized extracellular. Peroxisomes contain 50 or more enzymes and play a key role in fatty acid catabolism.[63,64] Peroxisome proliferator-activated receptors (PPAR) are a family of nuclear receptors that bind directly to fatty acids and are transcription factors that regulate expression of lipid-metabolizing enzymes. PPARs can regulate peroxisome proliferation and also play a role in adipogenic differentiation.[65] Although it is clear that cell function and cell metabolism are linked, the exact role of changes in hBMSC metabolism during the differentiation process will require further investigation. Changes in metabolism can affect the secondary metabolites available for anabolism, the oxygen requirements (hypoxia), and the rate (and efficiency) of ATP generation.

CONCLUSIONS

Culture of hBMSCs on nanofiber scaffolds influenced the cell and organelle shape, with all organelles having greater 3D character (larger Z-Depth). On nanofibers, cells were smaller in volume and the peroxisomes occupied a larger volume fraction of the cell. Organelles were positioned closer to the geometric center of the cell during nanofiber culture. Bioassays measurements indicated that peroxidase activity was increased on nanofibers. Thus, nanofiber effects on cell function and differentiation may be mediated by changes to cell and organelle shape, which may affect organelle functional capacity, reaction kinetics, and/or transport.

ACKNOWLEDGMENTS

WT was supported by a NIST-NRC Research Associateship. The hBMSCs employed in this work were provided by the Texas A&M Health Science Center College of Medicine Institute for Regenerative Medicine at Scott & White through a grant from NCRR of the NIH. The "standard deviation" (S.D.) is the same as the "combined standard uncertainty of the mean" for the purposes of this work. This article, a contribution of NIST, is not subject to US copyright. Certain equipment and instruments or materials are identified in the article to adequately specify the experimental details. Such identification does not imply recommendation by NIST, nor does it imply the materials are necessarily the best available for the purpose.

REFERENCES

1. Mei Y, Saha K, Bogatyrev SR, Yang J, Hook AL, Kalcioglu ZI, Cho SW, Mitalipova M, Pyzocha N, Rojas F, Van Vliet KJ, Davies MC, Alexander MR, Langer R, Jaenisch R, Anderson DG. Combinatorial development of biomaterials for clonal growth of human pluripotent stem cells. Nat Mater 2010;9:768–778.
2. Engler AJ, Sen S, Sweeney HL, Discher DE. Matrix elasticity directs stem cell lineage specification. Cell 2006;126:677–689.
3. Dalby MJ, Gadegaard N, Tare R, Andar A, Riehle MO, Herzyk P, Wilkinson CD, Oreffo RO. The control of human mesenchymal cell differentiation using nanoscale symmetry and disorder. Nat Mater 2007;6:997–1003.

4. Simon CG Jr, Yaszemski MJ, Ratcliffe A, Tomlins P, Luginbuehl R, Tesk JA. ASTM international workshop on standards and measurements for tissue engineering scaffolds. J Biomed Mater Res B Appl Biomater 2015;103:949–959.
5. Li WJ, Laurencin CT, Caterson EJ, Tuan RS, Ko FK. Electrospun nanofibrous structure: A novel scaffold for tissue engineering. J Biomed Mater Res 2002;60:613–621.
6. Mo XM, Xu CY, Kotaki M, Ramakrishna S. Electrospun P(LLA-CL) nanofiber: A biomimetic extracellular matrix for smooth muscle cell and endothelial cell proliferation. Biomaterials 2004;25:1883–1890.
7. Raya-Rivera A, Esquiliano DR, Yoo JJ, Lopez-Bayghen E, Soker S, Atala A. Tissue-engineered autologous urethras for patients who need reconstruction: An observational study. Lancet 2011;377: 1175–1182.
8. Del GC, Baiguera S, Ajalloueian F, Bianco A, Macchiarini P. Are synthetic scaffolds suitable for the development of clinical tissue-engineered tubular organs? J Biomed Mater Res 2014;102:2427–2447.
9. Elias KL, Price RL, Webster TJ. Enhanced functions of osteoblasts on nanometer diameter carbon fibers. Biomaterials 2002;23:3279–3287.
10. Smith LA, Liu X, Hu J, Ma PX. The influence of three-dimensional nanofibrous scaffolds on the osteogenic differentiation of embryonic stem cells. Biomaterials 2009;30:2516–2522.
11. Smith LA, Liu X, Hu J, Wang P, Ma PX. Enhancing osteogenic differentiation of mouse embryonic stem cells by nanofibers. Tissue Eng Part A 2009;15:1855–1864.
12. Ruckh TT, Kumar K, Kipper MJ, Popat KC. Osteogenic differentiation of bone marrow stromal cells on poly(epsilon-caprolactone) nanofiber scaffolds. Acta Biomater 2010;6:2949–2959.
13. Kumar G, Tison CK, Chatterjee K, Pine PS, McDaniel JH, Salit ML, Young MF, Simon Jr CG. The determination of stem cell fate by 3D scaffold structures through the control of cell shape. Biomaterials 2011;32:9188–9196.
14. Liu W, Wei Y, Zhang X, Xu M, Yang X, Deng X. Lower extent but similar rhythm of osteogenic behavior in hBMSCs cultured on nanofibrous scaffolds versus induced with osteogenic supplement. ACS Nano 2013;7:6928–6938.
15. Farooque TM, Camp CH Jr, Tison CK, Kumar G, Parekh SH, Simon CG Jr. Measuring stem cell dimensionality in tissue scaffolds. Biomaterials 2014;35:2558–2567.
16. Baker BA, Pine PS, Chatterjee K, Kumar G, Lin NJ, McDaniel JH, Salit ML, Simon Jr CG. Ontology analysis of global gene expression differences of human bone marrow stromal cells cultured on 3D scaffolds or 2D films. Biomaterials 2014;35:6716–6726.
17. Folkman J, Moscona A. Role of cell shape in growth control. Nature 1978;273:345–349.
18. Watt FM, Jordan PW, O'Neill CH. Cell shape controls terminal differentiation of human epidermal keratinocytes. Proc Natl Acad Sci USA 1988;85:5576–5580.
19. Chen CS, Mrksich M, Huang S, Whitesides GM, Ingber DE. Geometric control of cell life and death. Science 1997;276:1425–1428.
20. McBeath R, Pirone DM, Nelson CM, Bhadriraju K, Chen CS. Cell shape, cytoskeletal tension, and RhoA regulate stem cell lineage commitment. Dev Cell 2004;6:483–495.
21. Hakkinen KM, Harunaga JS, Doyle AD, Yamada KM. Direct comparisons of the morphology, migration, cell adhesions, and actin cytoskeleton of fibroblasts in four different three-dimensional extracellular matrices. Tissue Eng Part A 2011;17:713–724.
22. Ribeiro A, Vargo S, Powell EM, Leach JB. Substrate three-dimensionality induces elemental morphological transformation of sensory neurons on a physiologic timescale. Tissue Eng Part A 2012;18:93–102.
23. Khetan S, Guvendiren M, Legant WR, Cohen DM, Chen CS, Burdick JA. Degradation-mediated cellular traction directs stem cell fate in covalently crosslinked three-dimensional hydrogels. Nat Mater 2013;12:458–465.
24. Dominici M, Le BK, Mueller I, Slaper-Cortenback I, Marini F, Krause D, Deans R, Keating A, Prockop D, Horwitz E. Minimal criteria for defining multipotent mesenchymal stromal cells. The International Society for Cellular Therapy position statement. Cytotherapy 2006;8:315–317.
25. Poot M, Zhang YZ, Kramer JA, Wells KS, Jones LJ, Hanzel DK, Lugade AG, Singer VL, Haugland RP. Analysis of mitochondrial morphology and function with novel fixable fluorescent stains. J Histochem Cytochem 1996;44:1363–1372.
26. Kilgore JA, Dolman NJ, Davidson MW. A review of reagents for fluorescence microscopy of cellular compartments and structures, Part II: Reagents for non-vesicular organelles. Curr Protoc Cytom 2013:66:Unit 12.31.
27. Dolman NJ, Kilgore JA, Davidson MW. A review of reagents for fluorescence microscopy of cellular compartments and structures, Part I: BacMam labeling and reagents for vesicular structures. Curr Protoc Cytom 2013;12:Unit 12.30.
28. Kilgore JA, Dolman NJ, Davidson MW. A review of reagents for fluorescence microscopy of cellular compartments and structures, Part III: Reagents for actin, tubulin, cellular membranes, and whole cell and cytoplasm. Curr Protoc Cytom 2014;67:Unit 12.32.
29. Schneider CA, Rasband WS, Eliceiri KW. NIH Image to ImageJ: 25 years of image analysis. Nat Methods 2012;9:671–675.
30. Bolte S, Cordelieres FP. A guided tour into subcellular colocalization analysis in light microscopy. J Microsc 2006;224:213–232.
31. Ahn SJ, Costa J, Emanuel JR. PicoGreen quantitation of DNA: Effective evaluation of samples pre- or post-PCR. Nucleic Acids Res 1996;24:2623–2625.
32. Zhou M, Diwu Z, Panchuk-Voloshina N, Haugland RP. A stable nonfluorescent derivative of resorufin for the fluorometric determination of trace hydrogen peroxide: Applications in detecting the activity of phagocyte NADPH oxidase and other oxidases. Anal Biochem 1997;253:162–168.
33. Lin S, Cohen HP. Measurement of adenosine triphosphate content of crayfish stretch receptor cell preparations. Anal Biochem 1968; 24:531–540.
34. Berridge MV, Herst PM, Tan AS. Tetrazolium dyes as tools in cell biology: New insights into their cellular reduction. Biotechnol Annu Rev 2005;11:127–152.
35. Marbach EP, Weil MH. Rapid enzymatic measurement of blood lactate and pyruvate. Use and significance of metaphosphoric acid as a common precipitant. Clin Chem 1967;13:314–325.
36. Weiss P, Garber B. Shape and movement of mesenchyme cells as functions of the physical structure of the medium. contributions to a quantitative morphology. Proc Natl Acad Sci USA 1952;38: 264–280.
37. Zink D, Fischer AH, Nickerson JA. Nuclear structure in cancer cells. Nat Rev Cancer 2004;4:677–687.
38. Driscoll MK, Albanese JL, Xiong ZM, Mailman M, Losert W, Cao K. Automated image analysis of nuclear shape: What can we learn from a prematurely aged cell? Aging (Albany NY) 2012;4: 119–132.
39. Thomas CH, Collier JH, Sfeir CS, Healy KE. Engineering gene expression and protein synthesis by modulation of nuclear shape. Proc Natl Acad Sci USA 2002;99:1972–1977.
40. Khatau SB, Hale CM, Stewart-Hutchinson PJ, Patel MS, Stewart CL, Searson PC, Hodzic D, Wirtz D. A perinuclear actin cap regulates nuclear shape. Proc Natl Acad Sci USA 2009;106:19017–19022.
41. Wang B, Cai Q, Zhang S, Yang X, Deng X. The effect of poly (L-lactic acid) nanofiber orientation on osteogenic responses of human osteoblast-like MG63 cells. J Mech Behav Biomed Mater 2011;4:600–609.
42. Himeno-Ando A, Izumi Y, Yamaguchi A, Iimura T. Structural differences in the osteocyte network between the calvaria and long bone revealed by three-dimensional fluorescence morphometry, possibly reflecting distinct mechano-adaptations and sensitivities. Biochem Biophys Res Commun 2012;417:765–770.
43. Bidwell JP, Alvarez M, Feister H, Onyia J, Hock J. Nuclear matrix proteins and osteoblast gene expression. J Bone Miner Res 1998; 13:155–167.
44. Chambliss AB, Khatau SB, Erdenberger N, Robinson DK, Hodzic D, Longmore GD, Wirtz D. The LINC-anchored actin cap connects the extracellular milieu to the nucleus for ultrafast mechanotransduction. Sci Rep 2013;3:1087:1–9.
45. Merriman HL, van Wijnen AJ, Hiebert S, Bidwell JP, Fey E, Lian J, Stein J, Stein GS. The tissue-specific nuclear matrix protein, NMP-2, is a member of the AML/CBF/PEBP2/runt domain transcription factor family: Interactions with the osteocalcin gene promoter. Biochemistry 1995;34:13125–13132.

46. Cavalier-Smith T. Nuclear volume control by nucleoskeletal DNA, selection for cell volume and cell growth rate, and the solution of the DNA C-value paradox. J Cell Sci 1978;34:247–278.
47. Koch AL. What size should a bacterium be? A question of scale. Annu Rev Microbiol 1996;50:317–348.
48. Chan YH, Marshall WF. Scaling properties of cell and organelle size. Organogenesis 2010;6:88–96.
49. Lenski RE, Travisano M. Dynamics of adaptation and diversification: A 10,000-generation experiment with bacterial populations. Proc Natl Acad Sci USA 1994;91:6808–6814.
50. Philippe N, Pelosi L, Lenski RE, Schneider D. Evolution of penicillin-binding protein 2 concentration and cell shape during a long-term experiment with Escherichia coli. J Bacteriol 2009;191:909–921.
51. Lizana L, Bauer B, Orwar O. Controlling the rates of biochemical reactions and signaling networks by shape and volume changes. Proc Natl Acad Sci USA 2008;105:4099–4104.
52. Else PL, Hulbert AJ. Comparison of the "mammal machine" and the "reptile machine": Energy production. Am J Physiol 1981;240: R3–R9.
53. Gauthier NC, Rossier OM, Mathur A, Hone JC, Sheetz MP. Plasma membrane area increases with spread area by exocytosis of a GPI-anchored protein compartment. Mol Biol Cell 2009;20:3261–3272.
54. Figard L, Sokac AM. A membrane reservoir at the cell surface: Unfolding the plasma membrane to fuel cell shape change. Bioarchitecture 2014;4:39–46.
55. Rangamani P, Lipshtat A, Azeloglu EU, Calizo RC, Hu M, Ghassemi S, Hone J, Scarlata S, Neves SR, Iyengar R. Decoding information in cell shape. Cell 2013;154:1356–1369.
56. Meyers J, Craig J, Odde DJ. Potential for control of signaling pathways via cell size and shape. Curr Biol 2006;16:1685–1693.
57. Warburg O. On the origin of cancer cells. Science 1956;123:309–314.
58. DeBerardinis RJ, Lum JJ, Hatzivassiliou G, Thompson CB. The biology of cancer: Metabolic reprogramming fuels cell growth and proliferation. Cell Metab 2008;7:11–20.
59. Dang CV. The interplay between MYC and HIF in the Warburg effect. Ernst Schering Found Symp Proc 2007;4:35–53.
60. Facucho-Oliveira JM, Alderson J, Spikings EC, Egginton S, St John JC. Mitochondrial DNA replication during differentiation of murine embryonic stem cells. J Cell Sci 2007;120:4025–4034.
61. Folmes CD, Nelson TJ, Martinez-Fernandez A, Arrell DK, Lindor JZ, Dzeja PP, Ikeda Y, Perez-Terzic C, Terzic A. Somatic oxidative bioenergetics transitions into pluripotency-dependent glycolysis to facilitate nuclear reprogramming. Cell Metab 2011;14: 264–271.
62. Komarova SV, Ataullakhanov FI, Globus RK. Bioenergetics and mitochondrial transmembrane potential during differentiation of cultured osteoblasts. Am J Physiol Cell Physiol 2000;279:C1220–C1229.
63. Wanders RJ, Waterham HR. Biochemistry of mammalian peroxisomes revisited. Annu Rev Biochem 2006;75:295–332.
64. Smith JJ, Aitchison JD. Peroxisomes take shape. Nat Rev Mol Cell Biol 2013;14:803–817.
65. Tyagi S, Gupta P, Saini AS, Kaushal C, Sharma S. The peroxisome proliferator-activated receptor: A family of nuclear receptors role in various diseases. J Adv Pharm Technol Res 2011;2:236–240.